Fuel 191 (2017) 472–485

Contents lists available at ScienceDirect

Fuel

journal homepage: www.elsevier.com/locate/fuel

Full Length Article

Catalytic consequences of cation and anion substitutions on rate and mechanism of oxidative coupling of methane over hydroxyapatite catalysts

Su Cheun Oh [a], Yu Lei [b], Huiyong Chen [c], Dongxia Liu [a,*]

[a] Department of Chemical and Biomolecular Engineering, University of Maryland, College Park, MD 20742, United States
[b] Department of Chemical and Materials Engineering, The University of Alabama in Huntsville, 301 Sparkman Drive, Huntsville, AL 35899, United States
[c] School of Chemical Engineering, Northwest University, Xi'an, Shaanxi 710069, China

HIGHLIGHTS

- Pb^{2+}, F^- and both substitutions in hydroxyapatite (HAP) were studied.
- Both Pb^{2+} and F^- substitutions in HAP favored C_2H_6 formation.
- Kinetics of primary reactions on Pb-HAP and Pb-HAP-F was analyzed by Eley-Rideal mechanism.
- Kinetics of primary reactions on HAP and HAP-F was analyzed by Langmuir-Hinshelwood mechanism.
- Composition-catalytic performance correlations for HAP-based catalysts were established.

GRAPHICAL ABSTRACT

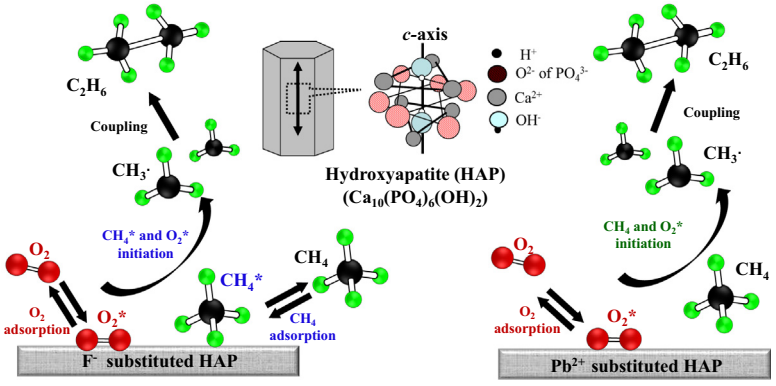

ARTICLE INFO

Article history:
Received 8 September 2016
Received in revised form 23 November 2016
Accepted 26 November 2016

Keywords:
Hydroxyapatite
Anion and cation substitution
Oxidative coupling of methane
Pb-hydroxyapatite
Kinetics

ABSTRACT

The identity and rate constants of elementary steps in primary reactions of oxidative coupling of methane (OCM) over Pb^{2+} and/or F^- substituted hydroxyapatite (HAP, Pb-HAP, HAP-F, and Pb-HAP-F) catalysts have been studied. The rigorous kinetics analysis suggests that HAP and HAP-F initiated the reaction between adsorbed methane and O_2 following Langmuir-Hinshelwood behavior. The Pb-HAP and Pb-HAP-F, however, enabled the reaction between gaseous methane and adsorbed O_2 in the Eley-Rideal mechanism. The F^- substitution of OH^- weakened both O_2 adsorption and C—H bond activation, leading to low methane conversion and slightly higher C_2H_6 selectivity. The substitution of Ca^{2+} by Pb^{2+} weakened both methane and oxygen adsorptions, but maintained C—H bond activation and raised C_2H_6 selectivity. The present analysis explored for the first time the effects of cation and/or anion in HAP on OCM reactions in which the analysis has been detailed and quantified in the nature of the mechanism-based kinetic models.

1. Introduction

The oxidative coupling of methane (OCM) involves the reaction of methane (CH_4) and oxygen (O_2) over a catalyst at high temperatures to form C_2 (C_2H_6 and C_2H_4) hydrocarbons. The nature of

* Corresponding author.
E-mail address: liud@umd.edu (D. Liu).

http://dx.doi.org/10.1016/j.fuel.2016.11.106
0016-2361/

one-step reaction to C_2 products in OCM reactions is of great significance and has been a continuous interest in the past few decades [1–4]. A variety of catalysts, including alkali [5–7], alkaline earth [8–12], rare earth [13–15] and transition metal oxides [16–18], have been broadly studied in OCM reactions. The general accepted mechanism of OCM reactions [19–21] is a mixed homogeneous-heterogeneous reaction network, in which methyl radicals ($CH_{3\cdot}$) are formed on the catalyst surface by methane activation, desorbed as free $CH_{3\cdot}$ radicals, and then recombined to form ethane (C_2H_6) as a primary product and ethylene (C_2H_4) as a secondary product from the subsequent dehydrogenation of C_2H_6. Simultaneously, methyl radicals undergo deep oxidation by adsorbed diatomic oxygen species and gas phase molecular oxygen (O_2), respectively, to produce CO_2 and CO.

Hydroxyapatite ($Ca_{10}(PO_4)_6(OH)_2$) is a type of calcium phosphate crystal, more commonly studied in biomaterials since it is the major component in bone and teeth [22,23]. The Ca^{2+} cation and the anion, either PO_4^{3-} or OH^-, in HAP can be substituted by other cations and/or anions to endow HAP with tunable thermal and chemical stability, catalytic properties, and ion/electronic conductivity [24–28]. Lead cation (Pb^{2+}) substituted HAP (Pb-HAP) has been studied as a catalyst for OCM reactions. It is shown that Pb-HAP was able to increase C_2 selectivity by a factor of ~5 compared to bare HAP [29–31]. The enhancement in OCM performance of Pb-HAP was ascribed to the stabilization of methyl radicals by Pb^{2+} sites for pairwise reactions against oxidation reactions [32]. The anion substitution such as halide-substituted HAP has been reported to enhance the acid resistance and mechanical properties of HAP bioceramics [33] and to reduce the number of oxygen species that are resulted from —OH groups in oxidative dehydrogenation of alkanes [34]. The substitution of HAP with both cation Pb^{2+} and fluoride anion (F^-) has not been explored in literature, but has potential to concurrently improve the thermal/chemical stability and catalytic activity of HAP in OCM reactions.

Selectivities and yields of C_2 products in OCM reactions depend on the identity and dynamics of specific elementary steps involved in the primary and secondary reaction steps on the catalysts. Even though the performance of Pb-HAP in OCM reactions has been studied and the enhancement in C_2 selectivity upon Pb^{2+} substitution in HAP has been justified [29,35], no rigorous kinetic study is available on the kinetics and mechanisms of OCM reactions on this catalyst. In addition, the effects of both cation and anion substituted HAP catalyst on the elementary steps of OCM reaction is yet to be determined. A detailed understanding of the kinetic networks is essential to describe the reaction steps in terms of their rate constants and to define the specific contributions of cation and anion compositions in HAP-based catalysts. On the basis of this understanding, a catalyst composition with desired catalytic performances can be developed for OCM reactions.

Herein, we report the synthesis and characterization of HAP catalysts with Pb^{2+} cation (Pb-HAP), F^- anion (HAP-F), and both cation and anion (Pb-HAP-F) substitutions. The influences of cation and/or anion substitutions in HAP on the rate and selectivity of OCM reactions together with identity and reaction rate constants of elementary steps in primary reactions of OCM were also examined. The results show that HAP and HAP-F followed Langmuir-Hinshelwood reaction pathway in which the reaction occurred between associatively adsorbed O_2 and CH_4 species. The Pb-HAP and Pb-HAP-F catalysts, however, followed Eley-Rideal reaction pathway in which the reaction occurred between gaseous CH_4 and associatively adsorbed O_2 species. The substitution of Ca^{2+} by Pb^{2+} in HAP preserved C—H activation in CH_4 and improved C_2 selectivity due to the stabilization of methyl radicals by Pb^{2+} sites for pairwise reaction despite impaired CH_4 and O_2 adsorption capabilities. The substitution of —OH groups by F^- in HAP weakened both O_2 adsorption and C—H bond activation compared to HAP, leading to low methane conversion and diminished CO_2 formation but higher C_2 selectivity. The Pb-HAP-F exhibited highest C_2 selectivity in the tested four HAP-based catalysts, which can be attributed to the integration of methyl radical pairwise reaction and reduced oxygen species on the catalyst in OCM reactions. The present study rigorously explored the mechanisms of OCM reactions and influences of cation and/or anion substitutions in HAP structure on the primary steps of these reactions.

2. Experimental

2.1. Materials

Ammonium phosphate dibasic ($(NH_4)_2HPO_4$, ⩾99.0%), ammonium chloride (NH_4Cl, ⩾99.5%), ammonium fluoride (NH_4F, A.C.S. Reagent, ⩾98.0%) and ammonia hydroxide solution (NH_4OH, 28–30%) were supplied from Sigma-Aldrich. Lead nitrate ($Pb(NO_3)_2$, ACS. Reagent) was purchased from J.T. Baker while calcium nitrate tetrahydrate ($Ca(NO_3)_2{\cdot}4H_2O$, 99.0–103.0%) was purchased from Alfa-Aesar.

2.2. HAP-based catalysts preparation

The synthesis of HAP-based catalysts was carried out by a co-precipitation method, as described in our previous work [36]. In the synthesis of bare HAP, 0.24 M of $(NH_4)_2HPO_4$ solution and 0.40 M of $Ca(NO_3)_2$ solution were prepared in two flasks separately. NH_4OH was added to each source solution to adjust the pH to ~10. $Ca(NO_3)_2$ solution was preheated to 363 K in an oil bath equipped with reflux condenser. After that, $(NH_4)_2HPO_4$ solution was added to the preheated $Ca(NO_3)_2$ solution dropwise via a syringe pump in 2 h. After addition of the $(NH_4)_2HPO_4$ solution, a cloudy reaction suspension was obtained and the suspension was kept at 363 K under magnetic stirring for 24 h followed by aging for 24 h at room temperature. Lastly, the product was collected by centrifugation at 6000 rpm for 5 min and washed with deionized (DI) water to remove any undesirable ions. The centrifugation and washing steps were repeated 5 times. The resulted wet product was dried in a vacuum oven at 343 K overnight.

As for the synthesis of HAP-F catalyst, the same procedure as that for bare HAP was applied except that a solution consisting of 0.16 M of $(NH_4)_2HPO_4$ and 0.08 M of NH_4F was prepared to replace 0.24 M of $(NH_4)_2HPO_4$ solution. In the synthesis of Pb-HAP-F catalyst, the $Ca(NO_3)_2$ solution used in bare HAP synthesis was replaced with a solution consisting of 0.32 M of $Ca(NO_3)_2$ and 0.08 M of $Pb(NO_3)_2$. The remaining procedures were the same as that for HAP-F catalyst. Pb-HAP was prepared using procedures reported previously [31], which was similar to the synthesis of bare HAP above except that an aqueous solution of $Pb(NO_3)_2$ (0.08 M), $Ca(NO_3)_2$ (0.32 M) and NH_4Cl (1.3 M) was prepared to replace 0.40 M of $Ca(NO_3)_2$ in HAP synthesis.

All the dried HAP-based catalysts were treated in flowing air (150 mL min^{-1}, ultrapure, Airgas) at 973 K for 5 h at a ramp rate of 17.5 K min^{-1} from room temperature. The catalyst samples were subsequently pelleted, crushed and sieved to retain particle sizes between 180 and 425 μm (40–80 mesh) for characterization and catalysis experiments discussed below.

2.3. Catalyst characterization

Scanning electron microscopy (SEM) images were taken on a Hitachi SU-70 electron microscope to visualize the morphologies of the HAP-based catalysts. N_2 adsorption-desorption isotherms of the samples were measured using an Autosorb-iQ analyzer (Quantachrome Instruments) at 77 K. The samples were outgassed

at 523 K for 8 h and 1 mmHg prior to measurements. Brunauer, Emmett and Teller (BET) method was used to determine the specific surface areas of the samples. X-ray diffraction (XRD) patterns of the catalyst samples were obtained on Bruker D8 Advance Lynx Powder Diffractometer (LynxEye PSD detector, sealed tube, Cu K_α radiation with Ni β-filter). The Fourier Transform Infrared (FTIR) spectra of the samples were recorded with a spectrometer (Nicolet Magna-IR 560) in the range of 400–4000 cm^{-1} with 36 scans and resolution of 4 cm^{-1}. The Raman spectra of the catalysts were collected with a Raman spectrometer (LabRAM Aramis, Horiba Scientific) in the range of 200–2000 cm^{-1}. Inductively coupled plasma optical emission spectroscopy (ICP-EOS, Optima 4300DV Instrument, Perkin-Elmer) was used to determine the elemental composition of the catalysts, specifically Pb, Ca and P contents. X-ray photoelectron spectroscopy (XPS) data was measured over a Kratos AXIS 165 spectrometer equipped with 165 mm radius hemispherical analyzer and eight channeltron detection system coupled with monochromatic Al radiation. C_{1s} peak was used to calibrate the binding energy of the products. The X-ray absorption fine structure spectroscopy (XAFS) measurements at Pb L_3 edge (~13.036 keV) were conducted at beamline 10-BM at the Advanced Photon Source in Argonne National Laboratory. XAFS data were collected in the transmission mode under ambient condition. PbO, PbO_2 and Pb foil were considered as references and measured at the beamline. The XAFS data were analyzed using IFEFFIT software package.

The oxygen temperature-programmed desorption (O_2-TPD) analysis of the catalyst samples were carried out in an Autosorb-iQ unit (Quantachrome, ASIQM0000-4) equipped with a thermal conductivity detector (TCD). Typically, 0.1 g catalyst sample was pretreated at 973 K for 2 h under He (40 mL min^{-1}, ultrapure, Airgas) at a heating rate of 10 K min^{-1} from ambient temperature. After being cooled to 353 K under He stream, O_2 stream (28 mL min^{-1}, ultrapure, Airgas) was introduced into the catalysts for 0.5 h. The adsorbed O_2 was then removed by flowing He gas (40 mL min^{-1}) for 2 h. Afterwards, the catalyst sample was ramped to 1100 K at a ramp rate of 10 K min^{-1} and the O_2-TPD profiles were recorded. The CH_4-TPD profiles of these catalysts were measured using the same procedure as O_2-TPD except that O_2 was switched to CH_4 in the measurement.

2.4. OCM catalytic test

The catalytic reaction was performed in a U-shape tubular quartz reactor (10 mm inner diameter). In the experiment, the catalyst sample was loaded in the quartz reactor in which the reactor was placed inside a temperature controlled furnace (National Electric Furnace FA120 type). The temperature of the furnace was controlled by a Watlow Controller (96 series). A K-type thermocouple was attached to the outer wall of the reactor to monitor the temperature of the catalyst environment. The catalyst was pretreated in He and O_2 atmosphere (33 mL min^{-1}, volume ratio: 91% He, 9% O_2) at 823 K for 5 h prior to the OCM reactions. The total gas flow rate was controlled at 46 mL min^{-1}, in which N_2 (5 mL min^{-1}, 99.95% purity, Airgas) was used as an internal standard and He was used as balance gas in all the experiments. Dependency of partial pressure of methane (P_{CH_4}) or partial pressure of oxygen (P_{O_2}) was examined by changing the flow rate of CH_4 or O_2 while keeping the flow rate of the other gas constant.

The reactant and product gases were analyzed using gas chromatograph (Agilent Technologies, 6890N) equipped with ShinCarbon ST packed column connected to a TCD. All the kinetics data were measured under differential conditions in which the methane conversion was maintained below 5%. The contribution of secondary reaction pathways was negligible since only the primary products (C_2H_6, CO and CO_2) were detected over the HAP-based catalysts. A blank test with the reactor without catalysts was carried out and the OCM result showed that methane conversion was less than 1%, implying that the gas phase reaction between CH_4 and O_2 was not favored under studied conditions.

3. Results and discussion

3.1. Structural analysis of HAP-based catalysts

Morphologies of the HAP-based catalysts were examined by SEM observation. Fig. 1 shows that bare HAP consists of short rod-shaped nanoparticles with sizes between 30 nm and 50 nm (Fig. 1(A)). Substitution of F^- and/or Pb^{2+} into HAP to form HAP-F (Fig. 1(B)), Pb-HAP-F (Fig. 1(C)) and Pb-HAP (Fig. 1(D)), respectively, did not change the morphologies significantly as short cylindrical-like nanoparticles can still be observed in these three samples. N_2 adsorption-desorption isotherms were used to reveal the surface areas of the HAP-based catalysts and the results are listed in Table 1. The cation and anion, or both cation and anion substitutions did not significantly change the morphology and surface areas of the HAP-based catalysts, which were all prepared by the co-precipitation method.

XRD, FTIR, Raman and XANES spectra were used to determine the crystallinity and incorporation of cations and/or anions into HAP-based catalysts, and the results are shown in Fig. 2. All peaks of the XRD spectra for HAP, HAP-F, Pb-HAP and Pb-HAP-F, respectively, in Fig. 2(A), are consistent with the crystalline HAP phase, indicating that HAP structure was well-preserved after the incorporation of cation (Pb^{2+}), anion (F^-), or both cation and anion (Pb^{2+} and F^{2-}), respectively. The downward shifting diffraction peaks of Pb-HAP and Pb-HAP-F with respect to HAP and HAP-F samples was caused by the incorporation of Pb^{2+}, which has larger size than Ca^{2+} and causes an expansion of the lattice parameters [31]. The broadening in width of the diffraction peaks in Pb-HAP-F and Pb-HAP samples suggests that the crystallinity of these two catalysts slightly decreased [37,38].

Fig. 2(B) demonstrates the FTIR spectra of HAP-based catalysts. All absorption bands characteristic for HAP [39] are shown in the spectra. The vibrational mode of OH^- group centered at 631 cm^{-1} indicates the presence of hydroxyl groups in the bare HAP and Pb-HAP samples. The absorption band at 631 cm^{-1} disappears in HAP-F and Pb-HAP-F, which could result from the substitution of OH^- by F^-, as evidenced by Bianco et al. [27]. Raman spectra in Fig. 2(C) are applied to further investigate the structural properties of the HAP-based catalysts. The vibrational modes of PO_4^{3-} groups, v_1 (~960–961 cm^{-1}), v_2 (~430–450 cm^{-1}), v_3 (~1035–1048 cm^{-1} and ~1070–1075 cm^{-1}) and v_4 (~587–604 cm^{-1}), are all well-preserved, which confirms the preservation of apatite structure in all the catalysts [40].

The oxidation state and possible phases of Pb ions in Pb-HAP and Pb-HAP-F were studied using Pb L_3 XANES spectra (Fig. 2(D)). PbO_2, Pb-HAP and Pb-HAP-F exhibited similar adsorption energies (E_0) at 13,039 eV. The ~3 eV shift to higher energy than the metallic Pb foil indicates that Pb-HAP is in higher oxidation state than zero. Pb L_3 edge represents mainly the 2p → 6p transition for Pb^{2+}-containing structures. On the other hand, a pre-edge at ~13,027 eV representing 2p → 6s transition can be observed for Pb^{4+} ions (e.g., PbO_2). The absence of pre-edge features in Pb-HAP and Pb-HAP-F XANES spectra indicates that most of the Pb ions in the catalysts are in the Pb^{2+} state. Detailed extended X-ray absorption fine structure (EXAFS) analysis of the reference lead oxides as well as the Pb^{2+} substituted HAP is summarized in Table 2 and Fig. 2(E) and (F). It is known that HAP has a hexagonal struc-

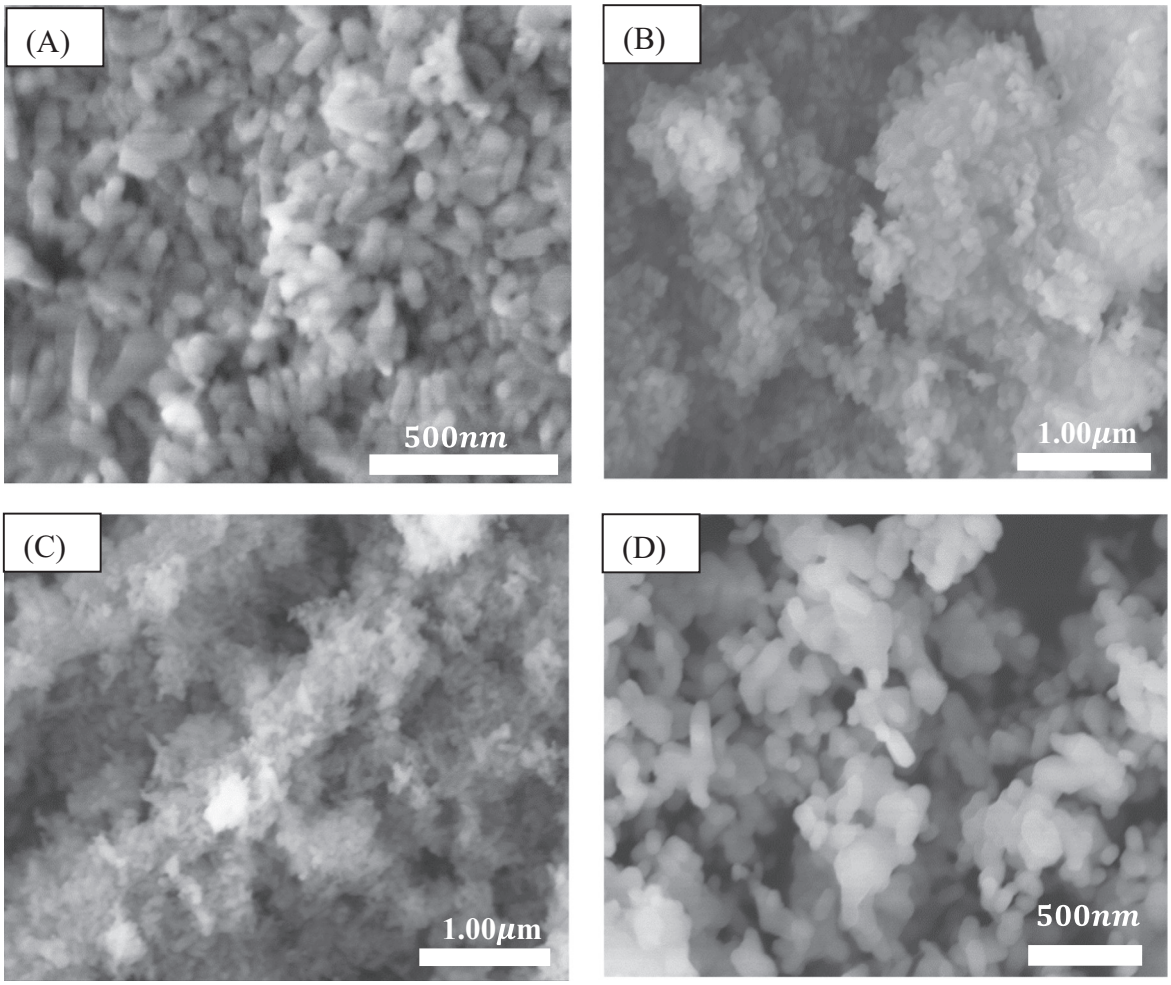

Fig. 1. SEM images showing morphologies of HAP-based catalysts: (A) HAP, (B) HAP-F, (C) Pb-HAP-F, (D) Pb-HAP, respectively.

Table 1
Chemical compositions and surface area of HAP-based catalysts for OCM reactions.

Catalyst	Composition measured by ICP			Composition measured by XPS				Surface area[a] (m^2/g)
	Pb/Ca	Pb/(Ca + Pb)	(Ca + Pb)/P	Pb/Ca	Pb/(Ca + Pb)	(Ca + Pb)/P	F/P	
HAP	0.00	0.00	1.72	0.00	0.00	1.59	0	39
HAP-F	0.00	0.00	1.73	0.00	0.00	1.76	0.58	25
Pb-HAP-F	0.25	0.20	1.80	0.50	0.33	1.97	0.62	24
Pb-HAP	0.25	0.20	1.66	0.47	0.32	1.63	0	29

[a] Determined by BET method.

ture that is comprised of 10 Ca^{2+} ions located on two sets of non-equivalent sites, 4 $Ca_{[1]}$ on site 1 and 6 $Ca_{[2]}$ on site 2 in one unit cell [43,44]. The $Ca_{[1]}$ is coordinated to 6 oxygen atoms belonging to different PO_4 tetrahedra and also to 3 oxygen atoms at a larger distance. The $Ca_{[2]}$ is found in cavities in the walls of the channels formed between the Ca and O atoms. The $Ca_{[2]}$ and then the $Ca_{[1]}$ can be subsequently substituted by Pb^{2+} ions with increasing concentrations [43,45]. The channels along c-axis of HAP, in which the OH^- anions reside, permit substitutional solid solution of some other anions such as F^- ions in the present study. In the present study, Pb partial substitutions of $Ca_{[2]}$ is most likely happened at low Pb loading and therefore fitted this work [43]. In Pb-HAP, Pb binds to about 4 oxygen atoms at a shorter distance (2.38 Å, 2.39 Å and 2.44 Å, respectively) and 3 oxygen atoms at a longer distance (2.51 Å and 2.72 Å). In Pb-HAP-F, Pb coordinates with 4 short distance oxygen and 3 long distance oxygen atoms. The substitution of OH^- by F^- sustainably also increases the Pb—O bond distance by ~0.1 Å compared to that in Pb-HAP.

3.2. Composition analysis of HAP-based catalysts

The bulk and surface compositions of the HAP-based catalysts were determined using ICP-OES and XPS analyses, and the results are listed in Table 1. The bulk (Ca + Pb)/P molar ratio in Pb-HAP is 1.66, nearly the same as the ratio of (Ca + Pb)/P = 1.67 in catalyst synthesis. For HAP, HAP-F and Pb-HAP-F samples, the (Ca + Pb)/P molar ratios are 1.72, 1.73 and 1.80, respectively, which are slightly higher than the starting ratio in the synthesis. The concentration of Pb^{2+} in both Pb-HAP and Pb-HAP-F catalyst samples is the same, indicated by the same Pb/Ca or Pb/(Ca + Pb) ratio in Table 1. The stoichiometry of HAP-based catalysts was slightly altered after the substitution of Pb^{2+} cation or F^- anion or both in the synthesis.

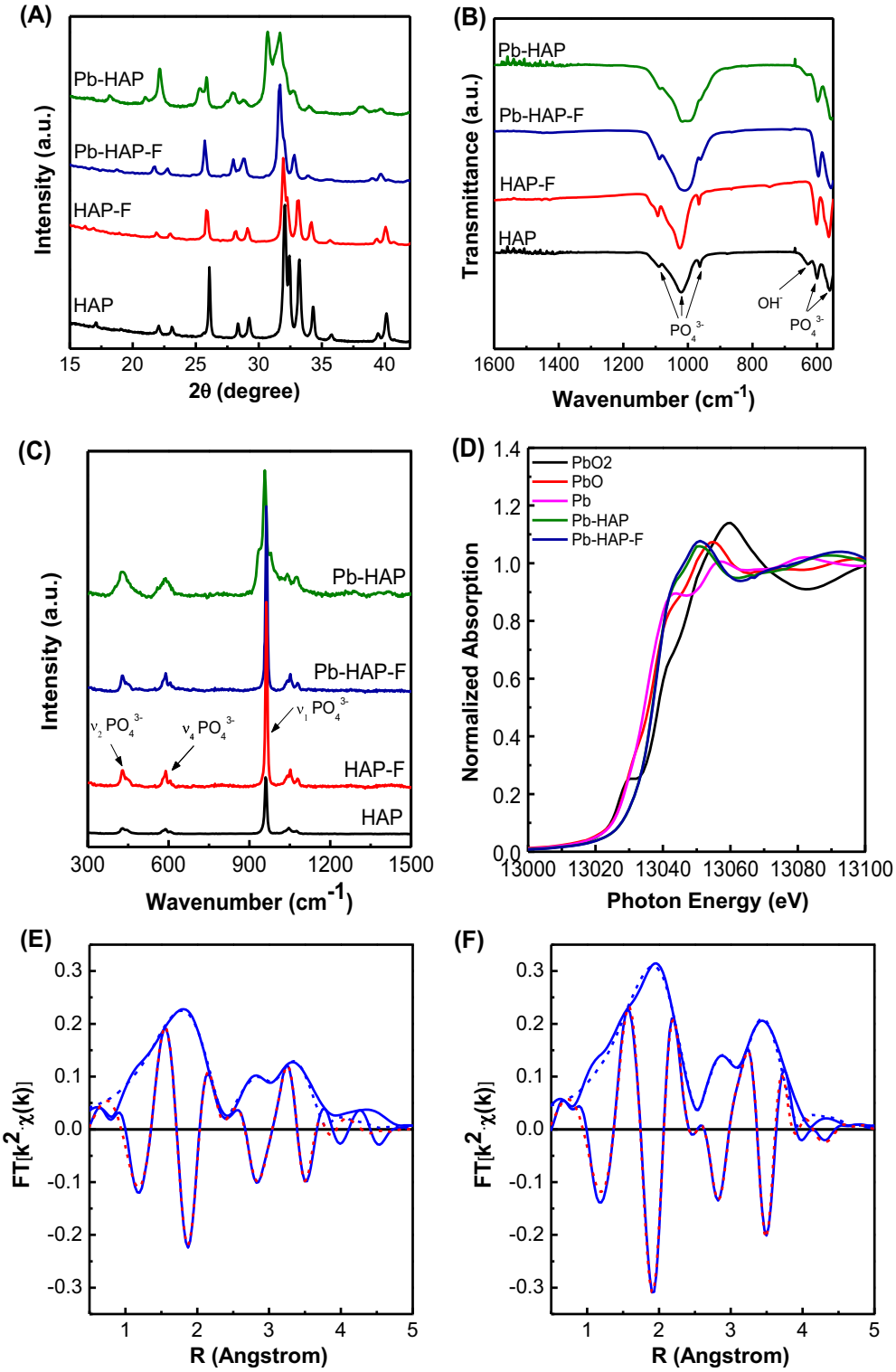

Fig. 2. XRD patterns (A), FT-IR spectra (B), Raman spectra (C), and XANES spectra (D) of HAP-based catalysts, respectively, used for OCM reactions. k^2-weighted magnitude and imaginary component of Fourier transform EXAFS of (E) Pb-HAP and (F) Pb-HAP-F. (k^2: Δk = 3–12 Å^{-1}. *Blue*, Fourier transform magnitude. *Red*, imaginary component. *Dash line*, experimental data. *Solid line*, fitted data). (For interpretation of the references to color in this figure legend, the reader should refer to the web version of this article.)

The surface composition of the HAP-based catalysts varied from their bulk composition. The surfaces of Pb-HAP-F and Pb-HAP catalysts were enriched with Pb^{2+} species since the Pb/Ca ratios were increased to 0.50 and 0.47 from 0.33 and 0.32, respectively (Table 1). The F^- concentrations, represented by F/P ratios, on the surfaces of HAP-F and Pb-HAP-F were similar.

3.3. O_2-TPD and CH_4-TPD profiles of HAP-based catalysts

Fig. 3 shows the O_2- and CH_4-TPD profiles in the temperature range of 300–1000 K. Two obvious desorption peaks were observed in all the catalysts in Fig. 3(A): one is in the lower temperature range of 350–650 K and the other one stays at higher temperatures

Table 2
EXAFS fit parameters for Pb oxides and Pb catalysts (k^2: $\Delta k = 3–12$ Å^{-1} and $\Delta r = 1.3–3.5$ Å).

Catalyst	N_{Pb-O}	R (Å)	DWF (Å^2)	E_0 (eV)
PbO	4	2.23	0.009	−5.5
PbO_2	2	2.15	0.004	−0.3
	4	2.19	0.004	−0.3
Pb-HAP	1.8	2.39	0.030	−7.7
	3.1	2.44	0.030	−7.7
	3.0	2.80	0.030	−7.7
Pb-HAP-F	2.5	2.49	0.031	−0.5
	2.5	2.55	0.031	−0.5
	3.0	2.91	0.031	−0.5

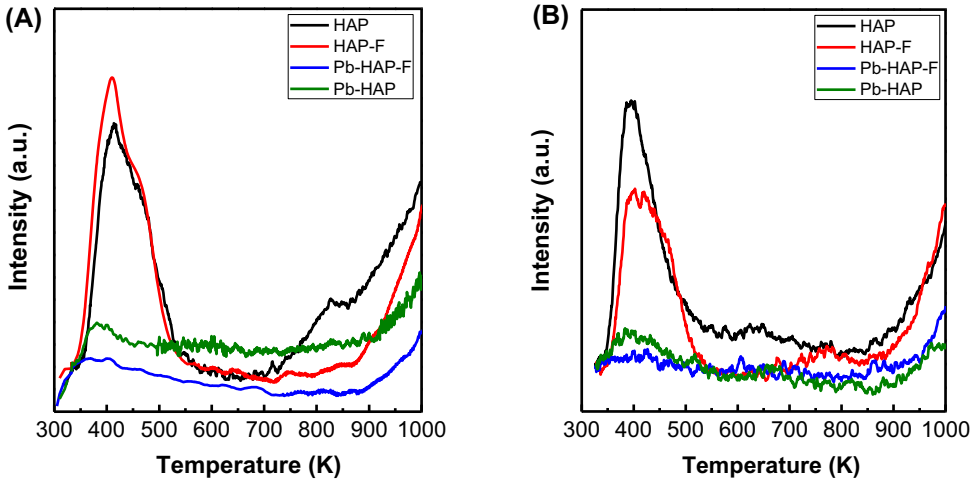

Fig. 3. O_2-TPD (A) and CH_4-TPD (B) profiles of HAP, HAP-F, Pb-HAP and Pb-HAP-F catalysts, respectively.

(>650 K). The O_2-TPD peak at lower temperature is ascribed to physisorbed oxygen while the higher one is attributed to chemisorbed oxygen species [41,42]. Both HAP and HAP-F catalysts showed very strong desorption peaks at both temperature ranges, suggesting that both catalysts have strong physi- and chemisorption of oxygen species. A close comparison of the O_2-TPD profiles between HAP and HAP-F shows that HAP-F has slightly higher physisorption of O_2 but distinctly lower chemisorption than that of HAP. The Pb^{2+} substitution in HAP structure drastically reduced O_2 adsorption, as indicated by the heavily reduced peak intensity in both temperature ranges in Fig. 3(A). The addition of F^- ions in Pb-HAP further reduced the physi- and chemisorption of O_2 species in HAP structure, as evidenced by the lowest peak intensities in all the tested samples.

The CH_4-TPD profiles in Fig. 3(B) show similar features to those of O_2-TPD profiles. Two desorption peaks (one below ~500 K and the other one above ~870 K) were observed in each catalyst. The intensity of both desorption peaks follows the order of HAP > HAP-F > Pb-HAP > Pb-HAP-F. Apparently, the substitution of Pb^{2+} and/or F^- ions deteriorated the adsorption capability of the HAP structure for CH_4 reactant. Pb^{2+} substitution of Ca^{2+} ions caused more critical influence on the adsorption capability than the F^- substitution of OH^- groups in the HAP-based catalyst materials.

The difference in O_2- and CH_4-TPD profiles in Fig. 3 across these four HAP-based catalysts should be correlated to their different cation and/or anion compositions and the resultant structural and physiochemical properties. Previous attempts [46–48] on understanding of oxygen species in HAP was conducted by electron spin resonance spectra after heating HAP to 1173 K followed by exposure to O_2. It was shown that O_2 could be adsorbed on either $Ca_{[2]}$ or dehydroxylated OH^- sites. The fluoroapatite (OH^- substituted by F^-) did not produce reactive oxygen species, which suggested no effective O_2 adsorption on the HAP-F material [49]. These results are consistent with the substantial decrease in the O_2-TPD peak in HAP-F and Pb-HAP-F compared to bare HAP in Fig. 3(A). The partial replacement of Ca^{2+} ions by Pb^{2+} caused significant drop in O_2-TPD peaks, suggesting that Ca^{2+} ions have better preference than Pb^{2+} in O_2 adsorption. The coincidence between the decrease in CH_4-TPD peaks and Pb^{2+} and/or F^- substitutions in HAP may indicate that CH_4 prefers to adsorb on Ca^{2+} and OH^- sites. Detailed mechanism for the observed TPD profiles needs further investigation.

3.4. Reaction pathways of OCM reactions over HAP-based catalysts

The kinetics of OCM reactions has been intensively studied over different catalysts [6,50–52]. A general accepted reaction network

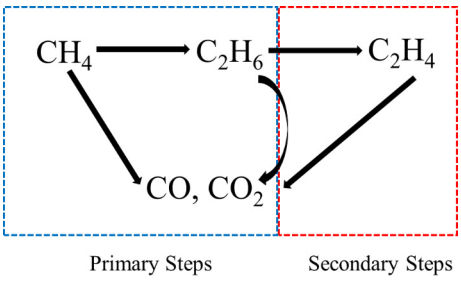

Scheme 1. General reaction pathway for oxidative coupling of methane. Only the primary reaction steps were considered in the present study.

(Scheme 1) has been proposed to account for the observed kinetics [53,54]. In this reaction network, activation of methane on catalysts leading to formation of methyl radicals and coupling of methyl radicals to form ethane are the primary reaction steps. The dehydrogenation of ethane to form ethylene is the secondary reaction step. The CO_x (CO and CO_2) can be formed via primary or secondary steps, as shown in Scheme 1. In the present study, we only focused on the primary reaction steps of OCM reactions.

The Eley-Rideal [55–61] and Langmuir-Hinshelwood [21,62–64] mechanisms have been commonly considered for the primary steps in OCM reactions. The Eley-Rideal mechanism states that the reaction between gaseous methane and adsorbed oxygen, either dissociative [57–59,65] or molecularly type [60,61], is the rate limiting step (RLS) in OCM reactions. An exemplary catalyst for this mechanism is 5%Na_2WO_4–2%Mn/SiO_2 [53,66–69]. The Langmuir-Hinshelwood mechanism regards RLS as the reaction between adsorbed methane and oxygen species. Sm_2O_3 [70], Na-doped MgO [63] and perovskite [64] catalysts have been proposed to follow this mechanism. The suitability of both mechanisms for OCM reactions over the HAP-based catalysts has been examined in the present study (refer to Supplementary Information). The kinetic data, however, suggests that the OCM reactions for HAP and HAP-F follow the Langmuir-Hinshelwood mechanism in which the RLS is the C—H bond activation between molecularly adsorbed methane and oxygen on two different active sites of these catalysts. For Pb-HAP and Pb-HAP-F, the OCM reactions follow the Eley-Rideal mechanism in which the RLS is the abstraction of hydrogen from gaseous methane by associatively adsorbed oxygen species on the catalysts.

3.4.1. Derivation of reaction rate equations

Scheme 2 shows the proposed reaction steps for OCM reactions over the HAP-based catalysts following the Langmuir-Hinshelwood mechanism. The reaction involves quasi-equilibrated associative oxygen adsorption on surface site 1 (^{*1}), leading to formation of O_2^{*1} species (step 1). Similarly, quasi-equilibrated associative adsorption of CH_4 on site 2 (^{*2}) results in CH_4^{*2} species (step 2). The reaction between adsorbed methane and oxygen forms methyl radicals (step 3, RLS). Under pseudo-steady state assumption for adsorbed O_2^{*1} and CH_4^{*2} species, the rate law for methane consumption (r_{CH_4}, μmol g_{cat}^{-1} s^{-1}) is shown in Eq. (1):

$$r_{CH_4} = k_3\left[K_1P_{O_2}\left(\frac{n_1}{(1+K_1P_{O_2})}\right)\right]\left[K_2P_{CH_4}\left(\frac{n_2}{(1+K_2P_{CH_4})}\right)\right] \quad (1)$$

where k_3 (μmol g_{cat} $[mol^{*1}]^{-1}$ $[mol^{*2}]^{-1}$ s^{-1}) is methane activation rate constant in step 3, K_1 (kPa^{-1}) and K_2 (kPa^{-1}) are the equilibrium constants for the adsorptions of oxygen (step 1) and methane (step 2), respectively. P_{CH_4} (kPa) and P_{O_2} (kPa) are the partial pressures of methane and oxygen in the reaction. n_1 (mol^{*1} g_{cat}^{-1}) and n_2 (mol^{*2} g_{cat}^{-1}) are the number of active sites for oxygen and methane adsorptions on the HAP-based catalysts. Details on the equation derivation can be referred to Section S2 of the Supplementary Information.

Scheme 3 shows the proposed reaction steps for OCM reactions over the HAP-based catalysts following the Eley-Rideal mechanism. The reaction involves quasi-equilibrated associative oxygen adsorption on surface site (*) to form O_2^* species (step 1). The reaction between gaseous methane and molecularly adsorbed oxygen forms methyl radicals (step 2, RLS). Under pseudo-steady state assumption for O_2^* species, the rate law for methane consumption (r_{CH_4}, μmol g_{cat}^{-1} s^{-1}) is shown in Eq. (2):

$$r_{CH_4} = k_3P_{CH_4}\left[K_1P_{O_2}\left(\frac{n_1}{(1+K_1P_{O_2})}\right)\right] \quad (2)$$

where k_3 (μmol $[mol^{*1}]^{-1}$ s^{-1} kPa^{-1}) is methane activation rate constant in step 2, K_1 (kPa^{-1}) is the equilibrium constant for the adsorption of oxygen (step 1), P_{CH_4} (kPa) and P_{O_2} (kPa) are the partial pressures of methane and oxygen in the reaction, n_1 (mol^{*1} g_{cat}^{-1}) is the number of active sites for O_2 adsorption in the catalyst. For consistency of rate constant notation in both Langmuir-Hinshelwood and Eley-Rideal mechanisms, k_3 is used (instead of k_2) to represent methane activation rate constant in step 2. Section S2 of the Supplementary Information detailed the derivation for Eq. (2).

The formation of primary products (C_2H_6, CO and CO_2) in both mechanisms are the same and is described by steps (4)–(6) in the Langmuir-Hinshelwood mechanism (Scheme 2) and by steps (3)–(5) in the Eley-Rideal mechanisms (Scheme 3). Methyl radicals couple with each other to form C_2H_6 (step 4 in Scheme 2 or step 3 in Scheme 3), but at the same time undergo side reactions with gaseous oxygen to form CO (step 5 in Scheme 2 or step 4 in Scheme 3) or adsorbed oxygen species to form CO_2 on the catalyst surface (step 6 in Scheme 2 or step 5 in Scheme 3). Under pseudo-steady-state assumption for methyl radicals, the rate law equations for C_2H_6 ($r_{C_2H_6}$, μmol g_{cat}^{-1} s^{-1}), CO (r_{CO}, μmol g_{cat}^{-1} s^{-1}) and CO_2 (r_{CO_2}, μmol g_{cat}^{-1} s^{-1}) formation are:

$$r_{C_2H_6} = k_4P_{CH_3\cdot}^2 \quad (3)$$

$$r_{CO} = k_5P_{CH_3\cdot}P_{O_2} \quad (4)$$

$$r_{CO_2} = k_6n_1P_{CH_3\cdot}\left[\frac{K_1P_{O_2}}{(1+K_1P_{O_2})}\right] \quad (5)$$

where k_4 (μmol g_{cat}^{-1} s^{-1} kPa^{-2}), k_5 (μmol g_{cat}^{-1} s^{-1} kPa^{-2}) and $k_6{\cdot}n_1$ (μmol g_{cat}^{-1} s^{-1} kPa^{-1}) are C_2H_6, CO and CO_2 formation rate constants, respectively, and $P_{CH_3\cdot}$ (kPa) is the partial pressure of methyl radicals with

$$P_{CH_3\cdot} = \frac{-\left[k_5P_{O_2}+\frac{k_6n_1K_1P_{O_2}}{(1+K_1P_{O_2})}\right]+\sqrt{\left[k_5P_{O_2}+\frac{k_6n_1K_1P_{O_2}}{(1+K_1P_{O_2})}\right]^2+4k_4K_1K_2k_3n_1n_2P_{CH_4}P_{O_2}\left(\frac{1}{(1+K_2P_{CH_4})}\right)\left(\frac{1}{(1+K_1P_{O_2})}\right)}}{2k_4}$$

for Langmuir-Hinshelwood mechanism and with

$$P_{CH_3\cdot} = \frac{-\left[k_5P_{O_2}+\frac{k_6n_1K_1P_{O_2}}{(1+K_1P_{O_2})}\right]+\sqrt{\left[k_5P_{O_2}+\frac{k_6n_1K_1P_{O_2}}{(1+K_1P_{O_2})}\right]^2+4k_4K_1k_3n_1P_{CH_4}P_{O_2}\left(\frac{1}{(1+K_1P_{O_2})}\right)}}{2k_4}$$

Step (1): $O_2 + *^1 \overset{K_1}{\leftrightarrow} O_2^{*1}$
Step (2): $CH_4 + *^2 \overset{K_2}{\leftrightarrow} CH_4^{*2}$
Step (3): $CH_4^{*2} + O_2^{*1} \overset{k_3}{\rightarrow} CH_3\cdot + HO_2\cdot + *^1 + *^2$ (RLS)
Step (4): $CH_3\cdot + CH_3\cdot \overset{k_4}{\rightarrow} C_2H_6$
Step (5): $CH_3\cdot + O_2 \overset{k_5}{\rightarrow} CO$
Step (6): $CH_3\cdot + O_2^{*1} \overset{k_6}{\rightarrow} CO_2$

Scheme 2. Proposed reaction steps based on Langmuir-Hinshelwood mechanism for OCM reactions over the HAP-based catalysts.

Step (1): $O_2 + * \overset{K_1}{\leftrightarrow} O_2^*$
Step (2): $CH_4 + O_2 * \overset{k_3}{\leftrightarrow} CH_3\cdot + HO_2\cdot + *$ (RLS)
Step (3): $CH_3\cdot + CH_3\cdot \overset{k_4}{\rightarrow} C_2H_6$
Step (4): $CH_3\cdot + O_2 \overset{k_5}{\rightarrow} CO$
Step (5): $CH_3\cdot + O_2^* \overset{k_6}{\rightarrow} CO_2$

Scheme 3. Proposed reaction steps based on Eley-Rideal mechanism for OCM reactions over the HAP-based catalysts.

for Eley-Rideal mechanism. The kinetic data were analyzed based on rate Eqs. (1)–(5) and are discussed below.

3.4.2. Methane and oxygen consumption rates over HAP-based catalysts based on Langmuir-Hinshelwood mechanism

The measured rates of CH_4 consumption as a function of P_{CH_4} and P_{O_2}, respectively, are shown in Fig. 4. The rate of CH_4 conversion increased with increasing P_{CH_4} and then gradually approached an upper limit (Fig. 4(A)) over these four HAP-based catalysts. The rate of CH_4 consumption exhibited a similar dependence on P_{O_2} (Fig. 4(B)). A comparison across these four catalysts showed that HAP enabled the highest methane conversion at the same P_{CH_4} or P_{O_2}, while HAP-F, Pb-HAP and Pb-HAP-F had similar but much lower conversions than the bare HAP catalyst.

The parameters in Eq. (1) were evaluated from kinetic data in Fig. 4. When P_{O_2} is fixed, Eq. (1) can be linearized as:

$$\frac{P_{CH_4}}{r_{CH_4}} = \frac{1}{k_3 n_1 n_2} \cdot \frac{1 + K_1 P_{O_2}}{K_1 P_{O_2}} \left(P_{CH_4} + \frac{1}{K_2} \right) \tag{6}$$

where the slope is $\frac{1+K_1P_{O_2}}{k_3 n_1 n_2 K_1 P_{O_2}}$ and the intercept is $\frac{1+K_1P_{O_2}}{k_3 n_1 n_2 K_1 K_2 P_{O_2}}$. The adsorption equilibrium constant for methane (K_2) was calculated from the ratio of slope to intercept in Eq. (6). Similarly, when P_{CH_4} is fixed in the measurement, the linear form of Eq. (1) can be written as:

$$\frac{P_{O_2}}{r_{CH_4}} = \frac{1}{k_3 n_1 n_2} \frac{1 + K_2 P_{CH_4}}{K_2 P_{CH_4}} \left(P_{O_2} + \frac{1}{K_1} \right) \tag{7}$$

The adsorption equilibrium constant for O_2 (K_1) was evaluated from the ratio of slope to intercept in Eq. (7). Substitution of K_1 and K_2 into Eqs. (6) or (7) led to the calculation for the product of $k_a = k_3 n_1 n_2$ ($\mu mol\ g_{cat}^{-1}\ s^{-1}$). Both Eqs. (5) and (6) can give k_a values ($k_{a,1}$ and $k_{a,2}$, respectively), which was averaged by $k_{a,avg} = (k_{a,1} + k_{a,2})/2$.

Fig. 5 shows the linearized correlations of $\frac{P_{CH_4}}{r_{CH_4}}$ versus P_{CH_4} (Fig. 5(A)) and $\frac{P_{O_2}}{r_{CH_4}}$ versus P_{O_2} (Fig. 5(B)), respectively. The linear fitting with coefficient of determination (R^2) > 0.96, positive intercept and slope in each set of kinetic data supports the proposed Langmuir-Hinshelwood mechanism for OCM reactions over the HAP-based catalysts. Table 3 shows that K_1 follows the sequence of HAP > HAP-F > Pb-HAP ~ Pb-HAP. This result is consistent with the O_2-TPD profiles of these four catalysts in Fig. 3(A). The K_2 values in Table 3 also follow the trend of HAP > HAP-F > Pb-HAP ~ Pb-HAP-F, consistent with the CH_4-TPD profiles (Fig. 3(B)) of these catalysts. The adsorption equilibrium constant reflects the bound nature of active species on the HAP-based catalysts. The bare HAP has the strongest oxygen and methane adsorption among these four catalysts. The F^- substitution in HAP significantly weakened O_2 adsorption (K_1 decreased by a factor of 3 compared to bare HAP) while only slightly influenced the methane adsorption. The Pb^{2+} substitution in HAP weakened both the oxygen and methane adsorption. The influence of Pb^{2+} substitution impaired the methane adsorption strength of HAP more significantly than F^-substitution (refer to K_2 values in Table 3). Pb-HAP-F showed similar K_1 and K_2 values to those of Pb-HAP catalyst. The C—H bond activation in step 3 of Scheme 2 (indicated by $k_{a,avg}$ in Table 3) over HAP catalyst was close to that of Pb-HAP catalyst. The F^- substitution in HAP apparently deteriorated the C—H activation of the HAP catalyst since HAP-F has ~4 times lower $k_{a,avg}$ than HAP or Pb-HAP. The co-existence of Pb^{2+} and F^- ions in HAP (Pb-HAP-F) only slightly sacrificed the C—H bond activation compared to Pb-HAP, suggesting that Pb^{2+} played an important role in contesting the sequestration effect of F^- ions on C—H bond activation in step 3 of the OCM reaction mechanism.

3.4.3. Methane and oxygen consumption rates over HAP-based catalysts based on Eley-Rideal mechanism

The K_2 values for Pb-HAP and Pb-HAP-F in Table 3 are significantly smaller (by a factor of ~6) compared to HAP and HAP-F, hinting that methane adsorption on the surface active sites for these two Pb-based catalysts is almost negligible. Eley-Rideal mechanism involving reaction between gaseous methane and adsorbed diatomic oxygen species was thus proposed to accommodate the OCM kinetics over these two catalysts. When P_{CH_4} is fixed, Eq. (2) can be linearized as:

$$\frac{P_{CH_4} n_1}{r_{CH_4}} = \frac{1}{k_3 K_1 P_{O_2}} + \frac{1}{k_3} \tag{8}$$

where the slope is $\frac{1}{k_3 n_1 K_1}$ and the intercept is $\frac{1}{k_3 n_1}$. The methane activation rate constant ($k_3 \cdot n_1$) and adsorption equilibrium constant for oxygen (K_1) were calculated from the intercept and slope in Eq. (8), respectively.

Fig. 6 shows the linearized correlations of $\frac{P_{CH_4}}{r_{CH_4}}$ versus $\frac{1}{P_{O_2}}$ (Fig. 6(A)). The linear fittings with R^2 > 0.97 support the proposed Eley-Rideal mechanism for OCM reactions over the HAP-based catalysts. Similar to Langmuir-Hinshelwood mechanism, Table 4 shows that K_1 follows the sequence of HAP > HAP-F > Pb-HAP ~ Pb-HAP,

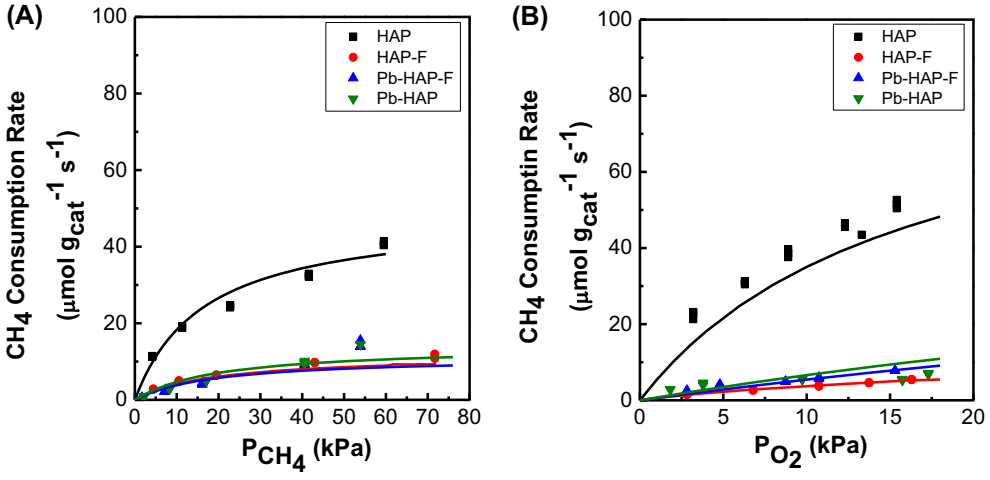

Fig. 4. Methane consumption rate as a function of CH_4 pressure at P_{O_2} = 7.0 kPa (A) and O_2 pressure at P_{CH_4} = 25 kPa (B), respectively. (973 K, 101 kPa total pressure, total flow rate = 46 mL min^{-1}, He as balance gas.) The curves in (A) and (B) denote the fitting results using optimized rate constants in Table 3.

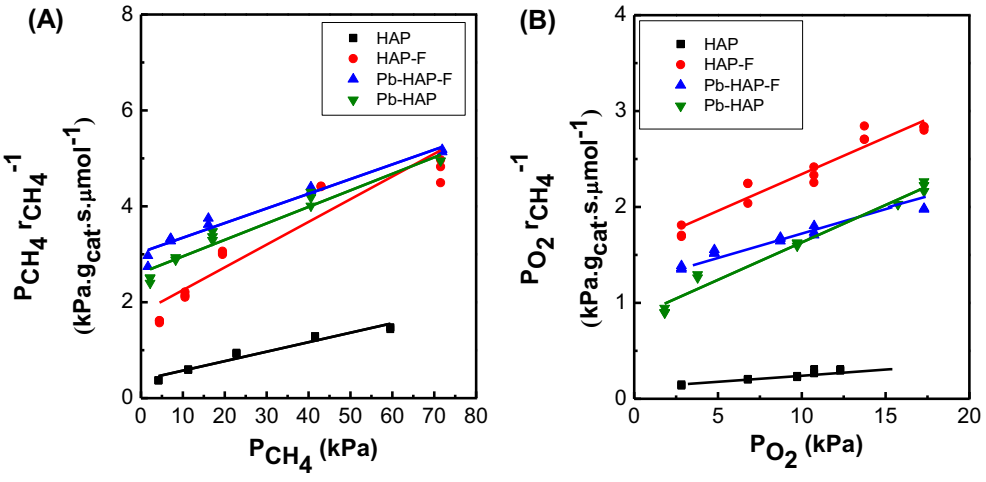

Fig. 5. Product of CH_4 pressure and the inverse rate of CH_4 consumption as a function of CH_4 pressure at fixed P_{O_2} = 7.0 kPa (A) and product of O_2 pressure and the inverse rate of CH_4 consumption as a function of O_2 pressure at fixed P_{CH_4} = 25 kPa (B) over HAP-based catalysts. (973 K, 101 kPa total pressure, total flow rate = 46 mL min^{-1}, He as balance gas.)

Table 3
Equilibrium constant of O_2 adsorption (K_1), equilibrium constant of CH_4 adsorption (K_2) and rate constant of CH_4 activation (k_a) based on Langmuir-Hinshelwood mechanism at 973 K of OCM reactions over HAP-based catalysts.

Catalyst	K_1[a] (kPa^{-1})	K_2[b] (kPa^{-1})	k_a[c] (μmol g_{cat}^{-1} s^{-1})	k_a[d] (μmol g_{cat}^{-1} s^{-1})	$k_{a,avg}$[e] (μmol g_{cat}^{-1} s^{-1})
HAP	0.11	0.063	116	88	102
HAP-F	0.040	0.052	43	49	47
Pb-HAP-F	0.032	0.010	68	84	76
Pb-HAP	0.032	0.010	90	100	95

[a] Errors are ±0.003 kPa^{-1}.
[b] Errors are ±0.004 kPa^{-1}.
[c] Determined by varying partial pressure of O_2.
[d] Determined by varying partial pressure of CH_4.
[e] $k_{a,avg} = (k_{a,1} + k_{a,2})/2$.

consistent with O_2-TPD profiles in Fig. 3(A). The C—H bond activation in step 3 of Scheme 3 (indicated by $k_3 \cdot n_1$ in Table 4) over HAP catalysts follows similar trend to that of Scheme 2 with Langmuir-Hinshelwood pathway. HAP has the highest methane activation rate constant, follows by Pb-HAP, Pb-HAP-F and HAP-F, respectively. Fig. 6(B) and (C) show fitting of the measured rates of CH_4 consumption as a function of P_{CH_4} and P_{O_2}, respectively using the Eley-Rideal model. The curves on the plots denote the fitting results using optimized K_1 and $k_3 \cdot n_1$ values in Table 4. The good fittings shown in Pb-HAP and Pb-HAP-F again suggests that these two catalysts leaned towards Eley-Rideal pathways with reaction between gaseous methane and adsorbed diatomic oxygen species. The poor fittings on HAP and HAP-F, on the other hand, explains that these two catalysts follow Langmuir-Hinshelwood pathways.

3.4.4. Product formation and selectivity over HAP-based catalysts

Fig. 7 shows C_2H_6, CO and CO_2 formation rates as a function of P_{CH_4} over the HAP-based catalysts. HAP exhibited slightly higher C_2H_6 formation rate among these four catalysts when P_{CH_4} was low, while Pb-HAP and Pb-HAP-F showed higher formation rates than bare HAP when P_{CH_4} was increased high enough (Fig. 7(A)). HAP-F has the lowest C_2H_6 formation rate compared to the other three catalysts. Fig. 7(B) shows the CO formation rate followed the order of HAP > HAP-F > Pb-HAP ~ Pb-HAP-F. The trend in CO_2 formation rate over these catalysts (Fig. 7(C)) is similar to that of CO formation. The kinetic data in Fig. 7 were used to obtain the regressed values for the rate constants k_4, k_5 and k_6 in Eqs. (3)–(5), respectively, and the fitted rate constants for each catalyst were listed in Table 5. For HAP and HAP-F, the values of K_1, K_2 and $k_{a,avg}$ in Table 3 (from Langmuir-Hinshelwood mechanism) were used for the regression to obtain product rate constants. For Pb-HAP and Pb-HAP-F, the values of K_1 and $k_3 \cdot n_1$ in Table 4 (from Eley-Rideal mechanism) were applied instead. The continuous curves in Fig. 7 denote the fitting results using the regressed rate constants for Eqs. (3)–(5). A R^2 values in all cases of above 0.90 suggests that the fitting for the experimental within error range is acceptable.

Fig. 8 shows the dependence of C_2H_6 selectivity on P_{CH_4} and P_{O_2} (represented by $\frac{r_{C_2H_6}}{(r_{CO_2}+r_{CO})}$) respectively, in the OCM reactions over the HAP-based catalysts. The C_2H_6 selectivity increased with increasing P_{CH_4} (Fig. 8(A)) and decreasing P_{O_2} (Fig. 8(B)). Higher methane pressure indicates lower O_2 concentration, which in turns slows down the oxidation of methane species to CO_x products. On the other hand, higher oxygen pressure promotes the oxidation reactions and thus leads to lower C_2H_6 selectivity. The dependence of C_2H_6 selectivity on P_{CH_4} and P_{O_2}, respectively, can be explicitly expressed by Eq. (9) that was derived from the rate equations for formation of C_2H_6, CO and CO_2 in steps (4)–(6) and steps (3)–(5) of the Langmuir-Hinshelwood and Eley-Rideal mechanisms, respectively.

$$\frac{r_{C_2H_6}}{r_{CO}+r_{CO_2}} = \frac{k_4 P_{CH_3}}{k_5 P_{O_2} + k_6 n_1 \left[\frac{K_1 P_{O_2}}{(1+K_1 P_{O_2})}\right]} \quad (9)$$

The curves in Fig. 8 denote the fitted results using optimized adsorption equilibrium constants and rate constants (K_1, K_2, $k_{a,avg}$, k_4, k_5 and k_6 in Tables 3 and 5 for HAP and HAP-F; K_1, $k_3 \cdot n_1$,

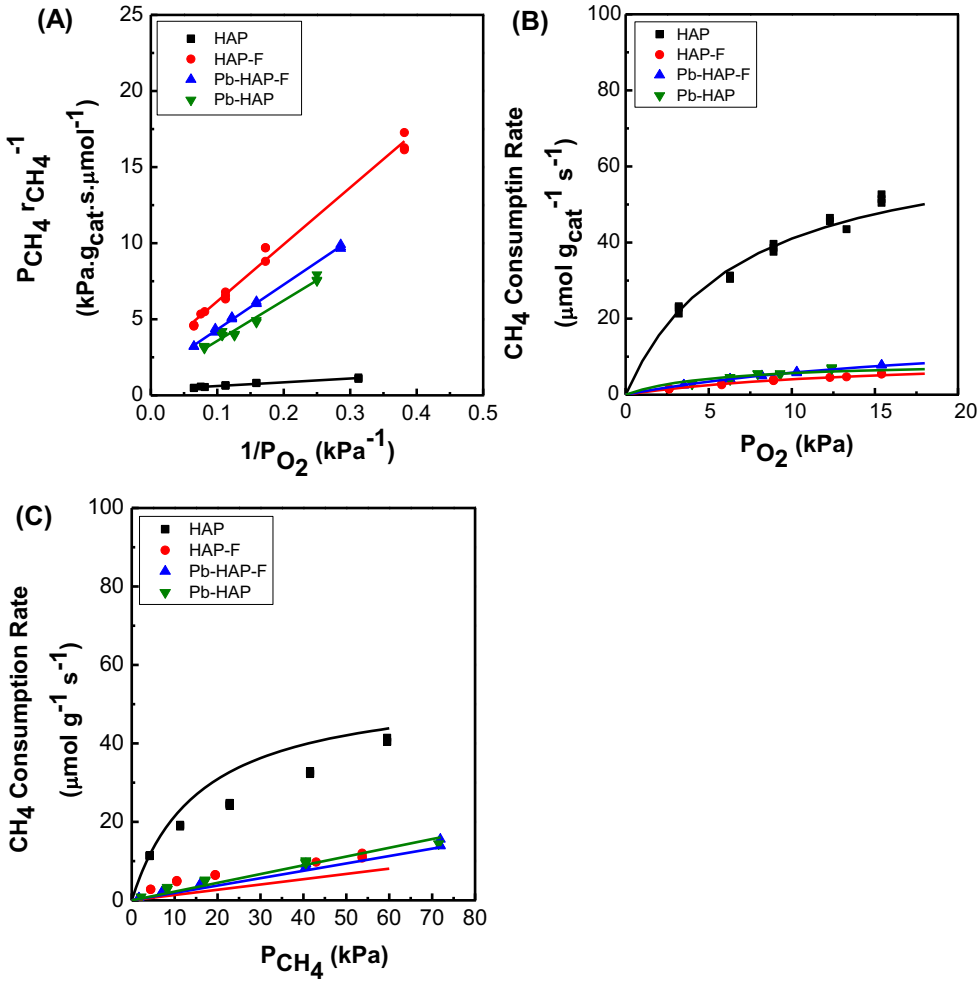

Fig. 6. Product of CH_4 pressure and the inverse rate of CH_4 consumption as a function of O_2 pressure at fixed P_{CH_4} = 25 kPa (A), methane consumption rate as a function of O_2 pressure at P_{CH_4} = 25 kPa (B) and CH_4 pressure at P_{O_2} = 7.0 kPa (C), respectively. (973 K, 101 kPa total pressure, total flow rate = 46 mL min^{-1}, He as balance gas.) The curves in (B) and (C) denote the fitting results using optimized rate.

Table 4
Equilibrium constant of O_2 adsorption (K_1) and rate constant of CH_4 activation ($k_3 \cdot n_1$) based on Eley-Rideal mechanism with associative O_2 adsorption at 973 K of OCM reactions over HAP-based catalysts.

Catalyst	K_1[a] (kPa^{-1})	$k_3 \cdot n_1$[b] (μmol g_{cat}^{-1} s^{-1} kPa^{-1})
HAP	0.15	2.77
HAP-F	0.07	0.41
Pb-HAP-F	0.04	0.77
Pb-HAP	0.04	1.02

[a] Errors are ±0.0015 kPa^{-1}.
[b] Errors are ±0.0035 μmol g_{cat}^{-1} s^{-1} kPa^{-1}.

k_4, k_5 and k_6 in Tables 4 and 5 for Pb-HAP and Pb-HAP-F). The Pb^{2+} substitution in HAP (either Pb-HAP or Pb-HAP-F) dramatically improved the primary C_2H_6 selectivity, consistent with previous reports [29,32,35,71] that Pb^{2+} ions favor pairwise reaction of methyl radicals while restricting the deep oxidation of methane species to CO_x. The comparison between Pb-HAP and Pb-HAP-F catalysts showed that C_2H_6 selectivity was slightly higher in Pb-HAP-F, suggesting that F^- substitution weakens O_2 adsorption, oxygen species formation and thus oxidation reactions. Therefore, C_2H_6 selectivity is improved. This conclusion applies to the comparison between HAP and HAP-F catalysts since the latter showed obviously higher C_2H_6 selectivity (Fig. 8).

The CO_2 or CO selectivity (defined as r_{CO_2}/r_{CO}) in the OCM reactions over the HAP-based catalysts has also been compared and the results are shown in Fig. 9. The preference for CO_2 formation versus CO in the oxidation reactions increased in the order of HAP-F < HAP < Pb-HAP < Pb-HAP-F. The ratio of r_{CO_2}/r_{CO} is independent of P_{CH_4} for each catalyst (Fig. 9(A)), suggesting that CO and CO_2 formation did not compete with each other even when CH_4 pressure was increased. The increase in O_2 pressure, however, led to a decrease in r_{CO_2}/r_{CO} over each catalyst. The degree of decrease in r_{CO_2}/r_{CO} as a function of O_2 pressure over the catalysts is in the order of HAP < HAP-F < Pb-HAP ~ Pb-HAP-F. According to the Langmuir-Hinshelwood mechanism proposed for OCM reactions over HAP and HAP-F and Eley-Rideal mechanism proposed for Pb-HAP and Pb-HAP-F in Schemes 2 and 3, respectively, CO_2 and CO formations result from the oxidation of methyl radical species by adsorbed diatomic oxygen species and gaseous oxygen, respectively. The relationship in terms of CO and CO_2 formation can be represented by Eq. (10), which was derived from the ratio of CO and CO_2 rate equations.

$$\frac{r_{CO_2}}{r_{CO}} = \frac{k_6 n_1 K_1}{k_5(1 + K_1 P_{O_2})} \quad (10)$$

The independence of r_{CO_2}/r_{CO} on CH_4 pressure in Eq. (10) is consistent with the kinetic data in Fig. 9(A). The P_{O_2} in the denominator of Eq. (10) suggests that r_{CO_2}/r_{CO} decreases with increasing O_2

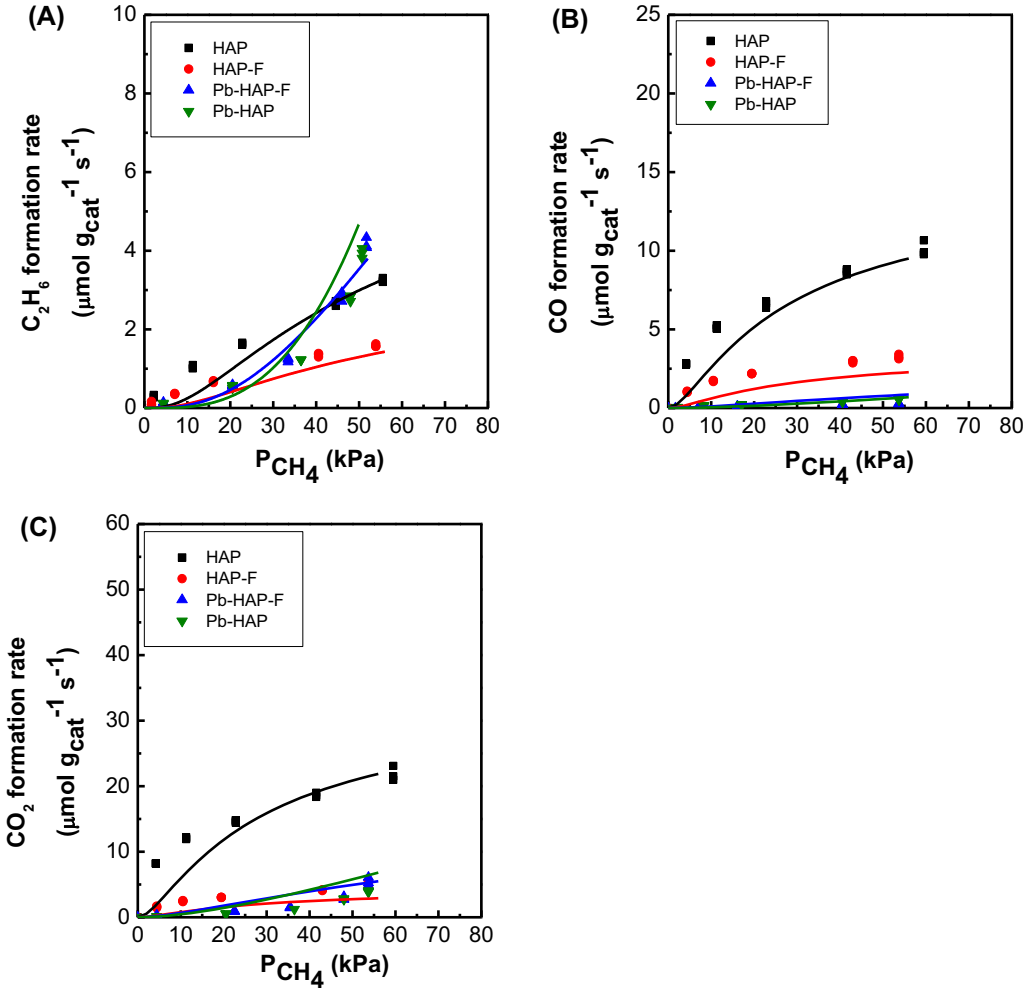

Fig. 7. C_2H_6 (A), CO (B) and CO_2 (C) formation rates as a function of CH_4 pressure at P_{O_2} = 7.0 kPa over HAP-based catalysts. (973 K, 101 kPa total pressure, total flow rate = 46 mL min^{-1}, He as balance gas.) The curves denote the fitting results using optimized rate constants.

Table 5
Rate constant for formation of C_2H_6 (k_4), CO (k_5) and CO_2 ($k_6 \cdot n_1$) at 973 K of OCM reactions over HAP-based catalysts.

Catalyst	k_4[c] (μmol g_{cat}^{-1} s^{-1} kPa^{-2})	k_5[d] (μmol g_{cat}^{-1} s^{-1} kPa^{-2})	$k_6 \cdot n_1$[e] (μmol g_{cat}^{-1} s^{-1} kPa^{-1})
HAP[a]	0.17	0.23	10.35
HAP-F[a]	0.50	0.20	8.01
Pb-HAP-F[b]	0.53	0.03	10.50
Pb-HAP[b]	0.45	0.03	9.50

[a] Determined from Langmuir-Hinshelwood mechanism.
[b] Determined from Eley-Rideal mechanism with associative O_2 adsorption.
[c] Errors are ±0.025 μmol g_{cat}^{-1} s^{-1} kPa^{-2}.
[d] Errors are ±0.0013 μmol g_{cat}^{-1} s^{-1} kPa^{-2}.
[e] Errors are ±0.7 μmol g_{cat}^{-1} s^{-1} kPa^{-1}.

pressure, which is consistent with data presented in Fig. 9(B). The different response of r_{CO_2}/r_{CO} with respect to O_2 pressure in each catalyst should be related to the kinetic parameters and the number of active sites for O_2 adsorption in Eq. (10). Apparently, the surfaces of Pb-HAP and Pb-HAP-F are very responsive to the changes of O_2 pressure in the OCM reactions.

3.4.5. Effects of Pb^{2+} and/or F^- substitution in HAP on OCM reactions

Selectivities and yields of C_2 products in OCM reactions depend on the identity and dynamics of primary steps that are dominated by the composition and physicochemical properties of the catalysts. Our study rigorously analyzed the primary reaction steps in terms of their adsorption equilibrium and rate constants and defined the specific contributions of cation and anion substitutions in HAP-based catalysts in these reaction steps. The measured kinetic data can be explained by the Langmuir-Hinshelwood mechanism for HAP and HAP-F and by Eley-Rideal mechanism for Pb-HAP and Pb-HAP-F. The product formation and selectivities were interpreted on the basis of this reaction mechanism together with the compositions of HAP-based catalysts.

The adsorption and formation of active oxygen species for OCM reactions mainly results from the dehydroxylation of OH^- groups ($Ca_{10}(PO_4)_6(OH)_2 \rightarrow Ca_{10}(PO_4)_6(OH)_{2-2x}O_x\square_x + xH_2O$, $\square$ = vacancy

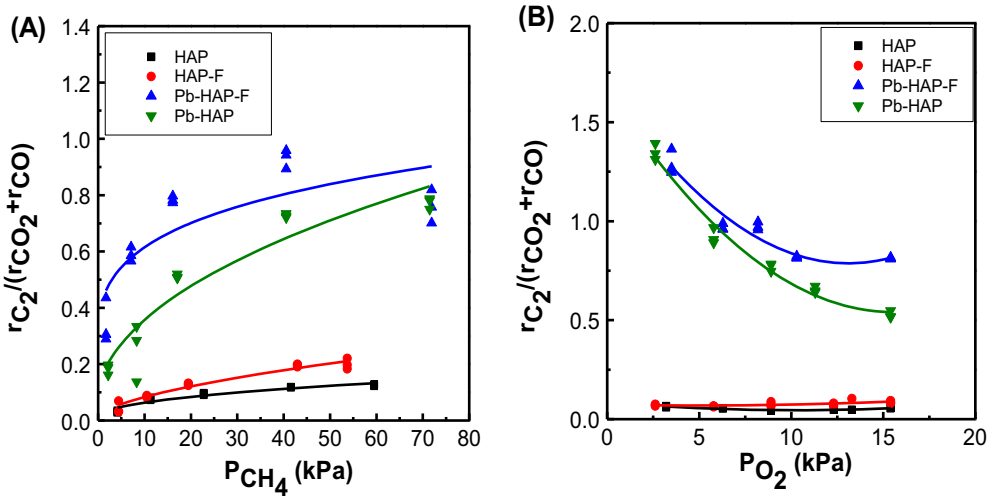

Fig. 8. C_2H_6 selectivity as a function of CH_4 pressure at P_{O_2} = 7.0 kPa (A) and as a function of O_2 pressure at P_{CH_4} = 25 kPa (B) over HAP-based catalysts. (973 K, 101 kPa total pressure, total flow rate = 46 mL min^{-1}, He as balance gas.) The curves denote the fitting results using optimized rate constants.

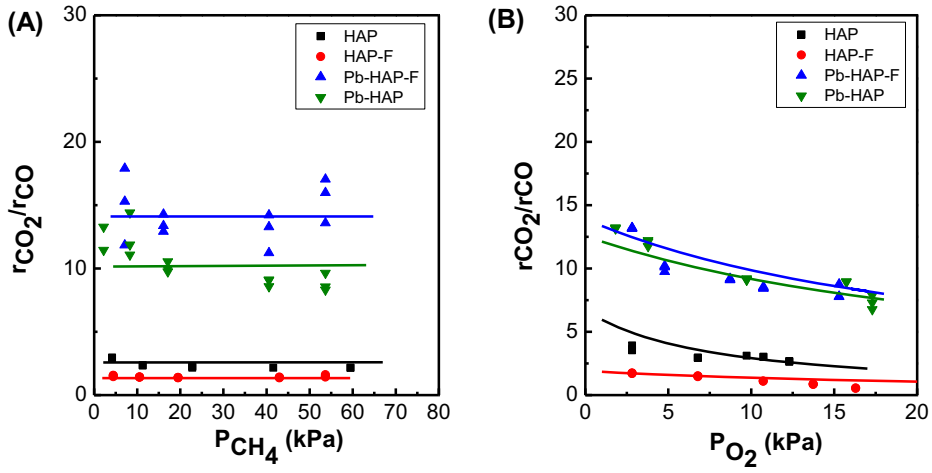

Fig. 9. CO_2 selectivity in oxidation reactions as a function of CH_4 pressure at P_{O_2} = 7.0 kPa (A) and as a function of O_2 pressure at P_{CH_4} = 25 kPa (B) over HAP-based catalysts. (973 K, 101 kPa total pressure, total flow rate = 46 mL min^{-1}, He as balance gas.) The curves denote the fitting results using optimized rate constants.

and x < 1) in the HAP-based catalysts under reaction temperatures, as the studies reported for activation of alkane in oxidation or oxidative dehydrogenation of alkanes over HAP catalyst [72,73]. The number of the OH^- groups, therefore, directly influences the oxygen adsorption, rate of oxygen consumption, C—H bond activation, rates of CO_x formation and selectivity in oxidation of methyl species to CO_x products. The F^- substitution of OH^- in HAP (HAP-F) decreased the number of OH^- groups and thus the number of active sites (n_1) and bonding strength for oxygen adsorption. As a result, the values of K_1 and $k_{a,avg}$ in steps (1) and (3) in proposed mechanisms of the OCM reactions were decreased. Therefore, lower reaction rates for methane and oxygen, as well as a higher C_2H_6 selectivity were observed in comparison to the bare HAP catalyst.

The substitution of Ca^{2+} by Pb^{2+} in HAP weakened both oxygen and methane adsorption, but did not deteriorate obviously C—H activation compared to bare HAP catalyst. Overall, the methane consumption rate was decreased and C_2H_6 selectivity was enhanced. The CO_2 selectivity in oxidation of methane species to CO_x was also favored. The enhancement in C_2H_6 selectivity can be due to the stabilization of methyl radicals by Pb^{2+} ions in the catalyst, as reported in previous studies [29,31,32,35,71]. The sequestration of CO_x formation due to the lower number of active oxygen species could contribute to the enhanced C_2H_6 selectivity. The weakening of oxygen and methane adsorption in HAP after Pb^{2+} substitution may be relevant to the altered coordination environment of cations in HAP structure. The concurrent substitutions of Ca^{2+} by Pb^{2+} and OH^- by F^- in Pb-HAP-F led to the highest C_2H_6 selectivity among the four studied HAP-based catalysts. Therefore, Pb-HAP-F coupled the beneficial influences of F^- and Pb^{2+} substitutions on OCM reactions.

The analysis between the composition, adsorption and catalytic performances (evaluated from O_2- and CH_4-TPD profiles, and K_1 and K_2 values in Table 3) of HAP-based catalysts endorsed the rationality to assign n_1 and n_2 as the number of OH^- and Ca^{2+} sites, respectively. The differentiation and correlation of adsorption sites in HAP-based materials for methane and oxygen species in OCM reactions have not been explored in literature. It should be noted that this assignment for n_1 and n_2 over the HAP-based catalysts in the present work may not be implicit enough since sole substitution of Ca^{2+} by Pb^{2+} or OH^- by F^- slightly affects the oxygen or methane adsorptions. The present study made initial attempt to understand the correlation between the composition and catalytic performance of HAP-based catalysts in OCM reactions.

4. Conclusions

The HAP structure with cation (Pb^{2+}), anion (F^-), or both (Pb^{2+} and F^-) substitutions have been synthesized. The cation and/or anion substitutions in HAP did not obviously change the morphological properties of the HAP-based materials. The catalytic OCM reactions over HAP with Pb^{2+} and/or F^- substitutions, however, was significantly influenced, which was reflected by the different oxygen and methane adsorption capabilities, C—H bond activation, CH_4 and O_2 consumption rates, C_2H_6 selectivity and CO_x formation interpreted by different reaction mechanisms. The substitution of Ca^{2+} by Pb^{2+} in HAP stabilized methyl radicals to favor their coupling for C_2H_6 formation compared to CO_x. The weakening of O_2 and CH_4 adsorption could also contribute to the enhancement in C_2H_6 selectivity. The F^- substitution of OH^- groups in HAP impaired O_2 adsorption and the concentration of active oxygen species, which led to a slight increase in C_2H_6 selectivtity and decrease in CO_x selectivity compared to bare HAP. The Langmuir-Hinshelwood mechanism with assumption of the reaction between molecularly adsorbed oxygen and methane species was proposed to accommodate the kinetic data for HAP and HAP-F. Eley-Rideal mechanism with assumption of reaction between gaseous methane and molecularly adsorbed oxygen species, on the other hand, was proposed to accommodate the kinetic data for Pb-HAP and Pb-HAP-F. The kinetic parameters in primary steps of OCM reactions for reactant consumption, product formation and selectivity were evaluated and interpreted on the basis of HAP-based catalyst composition. The present study explored for the first time the dynamics and identity of primary steps in OCM reactions that account for the correlations among composition-structure-catalytic performance of the HAP-based catalysts.

Acknowledgements

The authors gratefully acknowledge financial support from National Science Foundation (NSF-CBET 1264599 and 1351384). We acknowledge the support of Maryland NanoCenter and its NispLab. The NispLab is supported in part by the NSF as a MRSEC Shared Experimental Facility. MRCAT operations are supported by the Department of Energy and the MRCAT member institutions. This research used resources of the Advanced Photon Source, a U.S. Department of Energy (DOE) Office of Science User Facility operated for the DOE Office of Science by Argonne National Laboratory under Contract No. DE-AC02-06CH11357.

Appendix A. Supplementary material

The derivation of rate law equations for OCM reactions over the HAP-based catalysts according to (1) Eley-Rideal mechanism with reaction between gaseous methane and dissociative O_2 adsorption, (2) Eley-Rideal mechanism with reaction between gaseous methane and associative O_2 adsorption and (3) Langmuir-Hinshelwood mechanism with reaction between associatively adsorbed methane and associatively adsorbed O, respectively. Supplementary data associated with this article can be found, in the online version, at http://dx.doi.org/10.1016/j.fuel.2016.11.106.

References

[1] Hammond C, Conrad S, Hermans I. Oxidative methane upgrading. ChemSusChem 2012;5:1668–86.
[2] Arndt S, Laugel G, Levchenko S, Horn R, Baerns M, Scheffler M, et al. A critical assessment of Li/MgO-based catalysts for the oxidative coupling of methane. Catal Rev Sci Eng 2011;53:424–514.
[3] Lunsford JH. The catalytic oxidative coupling of methane. Angew Chem Int Ed 1995;34:970–80.
[4] Mleczko L, Baerns M. Catalytic oxidative coupling of methane—reaction engineering aspects and process schemes. Fuel Process Technol 1995;42:217–48.
[5] Otsuka K, Liu Q, Hatano M, Morikawa A. The catalysts active and selective in oxidative coupling of methane. alkali-doped samarium oxides. Chem Lett 1986;15:467–8.
[6] Miro E, Santamaria J, Wolf EE. Oxidative coupling of methane on alkali metal-promoted nickel titanate: I. Catalyst characterization and transient studies. J Catal 1990;124:451–64.
[7] Maiti GC, Baerns M. Dehydration of sodium hydroxide and lithium hydroxide dispersed over calcium oxide catalysts for the oxidative coupling of methane. Appl Catal, A 1995;127:219.
[8] DeBoy JM, Hicks RF. Oxidative coupling of methane over alkaline earth promoted La_2O_3. Chem Commun 1998;982–84.
[9] Dissanayake D, Lunsford JH, Rosynek MP. Oxidative coupling of methane over oxide-supported barium catalysts. J Catal 1993;143:286–98.
[10] Korf SJ, Roos JA, Veltman LJ, Ommen van JG, Ross JRH. Oxidative coupling of methane over chloride catalysts. Appl Catal 1989;56:119–29.
[11] Conway SJ, Greig JA, Thomas GM. Comparison of lanthanum oxide and strontium-modified lanthanum oxide catalysts for the oxidative coupling of methane. Appl Catal, A 1992;86:199–212.
[12] Carreiro JASP, Baerns M. Oxidative coupling of methane. J Catal 1989;117:258–65.
[13] Dedov AG, Loktev AS, Moiseev II, Aboukais A, Lamonier JF, Filimonov IN. Oxidative coupling of methane catalyzed by rare earth oxides: unexpected synergistic effect of the oxide mixtures. Appl Catal, A 2003;245:209–20.
[14] Van T, Che M, Kermarec M, Louis C, Tatibouët JM. Structure sensitivity of the catalytic oxidative coupling of methane on lanthanum oxide. Catal Lett 1990;6:395–400.
[15] Otsuka K, Jinno K. Kinetic studies on partial oxidation of methane over samarium oxides. Inorg Chim Acta 1986;121:237–41.
[16] Hatano M, Otsuka K. Alkali metal-doped transition metal oxides active for oxidative coupling of methane. Inorg Chim Acta 1988;146:243–7.
[17] Komatsu T, Amaya T, Otsuka K. LiCl doped cobalt oxide is an active catalyst for the formation of ethylene in the oxidative coupling of methane. Catal Lett 1989;3:317–22.
[18] Chan TK, Smith KJ. Oxidative coupling of methane over cobalt—magnesium and manganese—magnesium mixed oxide catalysts. Appl Catal 1990;60:13–31.
[19] Reyes SC, Iglesia E, Kelkar CP. Kinetic-transport models of bimodal reaction sequences—I. Homogeneous and heterogeneous pathways in oxidative coupling of methane. Chem Eng Sci 1993;48:2643–61.
[20] Reyes SC, Kelkar CP, Iglesia E. Kinetic-transport models and the design of catalysts and reactors for the oxidative coupling of methane. Catal Lett 1993;19:167–80.
[21] Korf SJ, Roos JA, Vreeman JA, Derksen JWHC, Ommen van JG, Ross JRH. A study of the kinetics of the oxidative coupling of methane over a Li/Sn/MgO. Catal Today 1990;6:417–26.
[22] Suchanek W, Yoshimura M. Processing and properties of hydroxyapatite-based biomaterials for use as hard tissue replacement implants. J Mater Res 1998;13:94–117.
[23] Liou S-C, Chen S-Y, Liu D-M. Manipulation of nanoneedle and nanosphere apatite/poly(acrylic acid) nanocomposites. J Biomed Mater Res B Appl Biomater 2005;73B:117–22.
[24] Matsuura Y, Onda A, Ogo S, Yanagisawa K. Acrylic acid synthesis from lactic acid over hydroxyapatite catalysts with various cations and anions. Catal Today 2014;226:192–7.
[25] Lee KY, Houalla M, Hercules DM, Hall WK. Catalytic oxidative decomposition of dimethyl methylphosphonate over Cu-substituted hydroxyapatite. J Catal 1994;145:223–31.
[26] Maiti GC, Freund F. Influence of fluorine substitution on the proton conductivity of hydroxyapatite. J Chem Soc Dalton Trans 1981:949–55.
[27] Bianco A, Cacciotti I, Lombardi M, Montanaro L, Bemporad E, Sebastiani M. F-substituted hydroxyapatite nanopowders: thermal stability, sintering behaviour and mechanical properties. Ceram Int 2010;36:313–22.
[28] Okazaki M, Miake Y, Tohda H, Yanagisawa T, Matsumoto T, Takahashi J. Functionally graded fluoridated apatites. Biomaterials 1999;20:1421–6.
[29] Matsumura Y, Moffat J. Catalytic oxidative coupling of methane over hydroxyapatite modified with lead. Catal Lett 1993;17:197–204.
[30] Lee KY, Han YC, Suh DJ, Park TJ. Pb-substituted hydroxyapatite catalysts prepared by coprecipitation method for oxidative coupling of methane. Stud Surf Sci Catal 1998;119:385–90.
[31] Park JH, Lee DW, Im SW, Lee YH, Suh DJ, Jun KW, et al. Oxidative coupling of methane using non-stoichiometric lead hydroxyapatite catalyst mixtures. Fuel 2012;94:433–9.
[32] Matsumura Y, Sugiyama S, Hayashi H, Moffat J. An apparent ensemble effect in the oxidative coupling of methane on hydroxyapatites with incorporated lead. Catal Lett 1994;30:235–40.
[33] Nathanael AJ, Mangalaraj D, Hong SI, Masuda Y, Rhee YH, Kim HW. Influence of fluorine substitution on the morphology and structure of hydroxyapatite nanocrystals prepared by hydrothermal method. Mater Chem Phys 2013;137:967–76.
[34] Sugiyama S, Hayashi H. Role of hydroxide groups in hydroxyapatite catalysts for the oxidative dehydrogenation of alkanes. Int J Mod Phys B 2003;17:1476–81.

[35] Matsumura Y, Sugiyama S, Hayashi H, Moffat JB. Lead-calcium hydroxyapatite: cation effects in the oxidative coupling of methane. J Solid State Chem 1995;114:138–45.
[36] Oh SC, Wu Y, Tran DT, Lee IC, Lei Y, Liu D. Influences of cation and anion substitutions on oxidative coupling of methane over hydroxyapatite catalysts. Fuel 2016;167:208–17.
[37] Kim SR, Lee JH, Kim YT, Riu DH, Jung SJ, Lee YJ, et al. Synthesis of Si, Mg substituted hydroxyapatites and their sintering behaviors. Biomaterials 2003;24:1389–98.
[38] Ren F, Leng Y, Xin R, Ge X. Synthesis, characterization and ab initio simulation of magnesium-substituted hydroxyapatite. Acta Biomater 2010;6:278796.
[39] Hongquan Z, Yuhua Y, Youfa W, Shipu L. Morphology and formation mechanism of hydroxyapatite whiskers from moderately acid solution. Mater Res 2003;6:111–5.
[40] Penel G, Delfosse C, Descamps M, Leroy G. Composition of bone and apatitic biomaterials as revealed by intravital Raman microspectroscopy. Bone 2005;36:893–901.
[41] Spinicci R, Tofanari A. Characterization of catalysts for methane-coupling by means of temperature programmed desorption. Catal Today 1990;6:473–9.
[42] Huang P, Zhao Y, Zhang J, Zhu Y, Sun Y. Exploiting shape effects of La_2O_3 nanocatalysts for oxidative coupling of methane reaction. Nanoscale 2013;5:10844–8.
[43] Ellis DE, Terra J, Warschkow O, Jiang M, Gonzalez GB, Okasinski JS, et al. A theoretical and experimental study of lead substitution in calcium hydroxyapatite. Phys Chem Chem Phys 2006;8:967–76.
[44] Sternlieb MP, Pasteris JD, Williams BR, Krol KA, Yoder CH. The structure and solubility of carbonated hydroxyl and chloro lead apatites. Polyhedron 2010;29:2364–72.
[45] Opre Z. Zürich: Swiss Fed. Inst. Technol. (ETH) Zurich; 2007. 171.
[46] Dugas J, Rey C. Electron spin resonance characterization of superoxide ions in some oxygenated apatites. J Phys Chem 1977;81:1417–9.
[47] Kazuhide M, Motoji I. Stabilization of radicals by doping from aqueous solutions into crystals of hydroxyapatite. Jpn J Appl Phys 1992;31:1353–7.
[48] Matsumura Y, Kanai H, Moffat JB. Formation of oxygen radicals by coordinatively unsaturated oxygen anions on hydroxyapatite. J Mol Catal A: Chem 1998;135:317–20.
[49] Kanai H, Lintuluoto M, Matsumura Y, Moffat JB. ESR study of the active oxygen species on hydroxyapatite activated by heat treatment. J Mol Catal A: Chem 2006;252:181–5.
[50] Index to volume 32. Catal Rev 1990;32:383.
[51] Amorebieta VT, Colussi AJ. Kinetics and mechanism of the catalytic oxidation of methane over lithium-promoted magnesium oxide. J Phys Chem 1988;92:4576–8.
[52] Lehmann L, Berns M. Kinetic studies of the oxidative coupling of methane over a NaOH/CaO catalyst. J Catal 1992;135:467–80.
[53] Takanabe K, Iglesia E. Mechanistic aspects and reaction pathways for oxidative coupling of methane on $Mn/Na_2WO_4/SiO_2$ catalysts. J Phys Chem C 2009;113:10131–45.
[54] Ghose R, Hwang HT, Varma A. Oxidative coupling of methane using catalysts synthesized by solution combustion method: catalyst optimization and kinetic studies. Appl Catal, A 2014;472:39–46.
[55] Beck B, Fleischer V, Arndt S, Hevia MG, Urakawa A, Hugo P, et al. Oxidative coupling of methane—a complex surface/gas phase mechanism with strong impact on the reaction engineering. Catal Today 2014;228:212–8.
[56] Wolf EE. Methane to light hydrocarbons via oxidative methane coupling: lessons from the past to search for a selective heterogeneous catalyst. J Phys Chem Lett 2014;5:986–8.
[57] Su YS, Ying JY, Green Jr WH. Upper bound on the yield for oxidative coupling of methane. J Catal 2003;218:321–33.
[58] Mallens EPJ, Hoebink JHBJ, Marin GB. An investigation of the oxygen pathways in the oxidative coupling of methane over MgO-based catalysts. J Catal 1996;160:222–34.
[59] Thybaut JW, Sun J, Olivier L, Van Veen AC, Mirodatos C, Marin GB. Catalyst design based on microkinetic models: oxidative coupling of methane. Catal Today 2011;159:29–36.
[60] Wolf D, Slinko M, Kurkina E, Baerns. Kinetic simulations of surface processes of the oxidative coupling of methane over a basic oxide catalyst. Appl Catal, A 1998;166:47–54.
[61] Tung WY, Lobban LL. Oxidative coupling of methane over lithium/magnesia: kinetics and mechanisms. Ind Eng Chem Res 1992;31:1621–5.
[62] Burch R, Tsang SC, Swarnakar R. Kinetic and mechanistic study of the methane coupling reaction. Faraday Trans 1990;86:3803–7.
[63] Iwamatsu E, Aika KI. Kinetic analysis of the oxidative coupling of methane over Na^+-doped MgO. J Catal 1989;117:416–31.
[64] Taheri Z, Seyed-Matin N, Safekordi AA, Nazari K, Pashne SZ. A comparative kinetic study on the oxidative coupling of methane over LSCF perovskite-type catalyst. Appl Catal, A 2009;354:143–52.
[65] Couwenberg PM, Chen Q, Marin GB. Kinetics of a gas-phase chain reaction catalyzed by a solid: the oxidative coupling of methane over Li/MgO-based catalysts. Ind Eng Chem Res 1996;35:3999.
[66] Sadjadi S, Jaso S, Godini HR, Arndt S, Wollgarten M, Blume R, et al. Feasibility study of the $Mn–Na_2WO_4/SiO_2$ catalytic system for the oxidative coupling of methane in a fluidized-bed reactor. Catal Sci Technol 2015;5:942–52.
[67] Wang DJ, Rosynek MP, Lunsford JH. Oxidative coupling of methane over oxide-supported sodium-manganese catalysts. J Catal 1995;155:390–402.
[68] Wang J, Chou L, Zhang B, Song H, Zhao J, Yang J, et al. Comparative study on oxidation of methane to ethane and ethylene over $Na_2WO_4–Mn/SiO_2$ catalysts prepared by different methods. J Mol Catal A: Chem 2006;245:272–7.
[69] Zhang H, Wu J, Qin S, Hu C. Study of the effect of gas space time on the combination of methane gas-phase oxidation and catalytic oxidative coupling over $Mn/Na_2WO_4/SiO_2$ Catalyst. Ind Eng Chem Res 2006;45:7090–5.
[70] Roos JA, Korf SJ, Veehof RHJ, Ommen van JG, Ross JRH. Kinetic and mechanistic aspects of the oxidative coupling of methane over a Li/MgO catalyst. Appl Catal 1989;52:131–45.
[71] Matsumura Y, Moffat JB, Sugiyama S, Hayashi H, Shigemoto N, Saitoh K. Selective oxidative coupling of methane catalysed over hydroxyapatite ion-exchanged with lead. J Chem Soc, Faraday Trans 1994;90:2133–40.
[72] Sugiyama S, Shono T, Makino D, Moriga T, Hayashi H. Enhancement of the catalytic activities in propane oxidation and H-D exchangeability of hydroxyl groups by the incorporation with cobalt into strontium hydroxyapatite. J Catal 2003;214:8–14.
[73] Sugiyama S, Osaka T, Hashimoto T, Sotowa KI. Oxidative dehydrogenation of propane on calcium hydroxyapatites partially substituted with vanadate. Catal Lett 2005;103:121–3.